# Ultrafast anisotropic disordering in graphite driven by intense hard X-ray pulses

N.J. Hartley[*,a,b], J. Grenzer[a], W. Lu[c], L.G. Huang[a], Y. Inubushi[d,e], N. Kamimura[f], K. Katagiri[f], R. Kodama[f,g,h,b], A. Kon[d,e], V. Lipp[i], M. Makita[c], T. Matsuoka[b], N. Medvedev[j,k], S. Nakajima[f], N. Ozaki[f,h], T. Pikuz[f,l], A.V. Rode[m], K. Rohatsch[a,n], D. Sagae[f], A.K. Schuster[a,n], K. Tono[d,e], J. Vorberger[a], T. Yabuuchi[d,e], D. Kraus[a,n]

[a] *Helmholtz-Zentrum Dresden-Rossendorf, Dresden 01328, Germany*
[b] *Open and Transdisciplinary Research Institute, Osaka University, Suita, Osaka 565-0087, Japan*
[c] *European XFEL GmbH, Schenefeld 22869, Germany*
[d] *RIKEN SPring-8 Center, Sayo, Hyogo 679-5148, Japan*
[e] *Japan Synchrotron Radiation Research Institute (JASRI), Sayo, Hyogo 679-5198, Japan*
[f] *Graduate School of Engineering, Osaka University, Suita, Osaka 565-0087, Japan*
[g] *Institute of Laser Engineering, Osaka University, Suita, Osaka 565-0871, Japan*
[h] *Photon Pioneers Center, Osaka University, Suita, Osaka 565-0087, Japan*
[i] *Center for Free-Electron Laser Science, DESY, Hamburg 22607, Germany*
[j] *Institute of Physics, Czech Academy of Sciences, Na Slovance 2, Prague 8, 18221, Czech Republic*
[k] *Institute of Plasma Physics, Czech Academy of Sciences, Prague 8, 18200, Czech Republic*
[l] *Joint Institute for High Temperatures, RAS, Moscow 125412, Russia*
[m] *Laser Physics Centre, RSPE, Australian National University, Canberra ACT0200, Australia*
[n] *Technische Universität Dresden, Dresden 01062, Germany*

## ARTICLE INFO

## ABSTRACT

We present results from the SPring-8 Angstrom Compact free electron LAser (SACLA) X-ray free electron laser (XFEL) facility, using an X-ray pump, X-ray probe scheme to observe ultrafast changes in the structure of heated graphite. The 9.8 keV XFEL beam was focused to give an intensity on the order of $\sim 10^{19}$ W/cm$^2$, and the evolution of the diffraction pattern observed up to delays of 300 fs. The interplanar diffraction peaks weaken significantly within 10s of femtoseconds, but in-plane diffraction orders i.e. those with Miller Index ($hk$0), persist up to 300 fs, with the observed signal increasing. We interpret this as nonthermal damage through the breaking of interplanar bonds, which at longer timescales leads to ablation by removal of intact graphite sheets. Post-experiment examination of the graphite samples shows damage which is comparable in size to the range of the excited photoelectrons. These results highlight the challenges of accurately modelling X-ray driven heating, as it becomes a routine approach to generating high energy density states.

## Introduction

Nonthermal melting on ultrafast timescales has been widely observed in semiconductors, where large numbers of electrons can be excited by femtosecond pulses of optical or infrared laser light [1–4]. In general, the energy deposition and subsequent evolution of the sample is a complex process [5,6], with highly nonequilibrium electron energy distributions [7,8] and consequent effects for the electron-ion energy exchange [9,10]. Samples can transiently reach new phases [11], passing through extreme pressures and temperatures [12], and so new approaches to understanding the interactions are of interest [13,14].

At the same time, the advent of X-ray free electron lasers (XFELs) has allowed far higher brilliances than previous X-ray sources, and together with new approaches to focusing the generated beams [15], allowing spot sizes of less than 1 μm, X-ray intensities comparable to those possible with optical lasers can now be reached [16]. This opens up a whole new way to drive such ultrafast heating. Unlike optical irradiation, an X-ray beam can penetrate deep into a target, isochorically heating a significant volume and driving it into a warm dense state [17]. The X-ray intensities now available are sufficient to induce

heating to nonequilibrium states [18], explosions [19] and ultrafast phase changes [20–22].

Although optical lasers can drive rapid ionization in semiconductors [23], X-rays are able to cause ionization in a much wider range of materials, due to their high photon energy. The X-ray energy is deposited by exciting photoelectrons and subsequent Auger cascades [24,25] which distribute energy across a wide range, through a variety of complex processes depending on material properties including the sample elements, stopping power, density and more. How the sample responds to this initially electronic excitation depends largely on the electronic and crystal structures, which can give rise to effects such as crystal mismatch heating [26], where non-close-packed structures will rapidly disorder after ionization. These nonthermal effects can occur on femtosecond timescales, and so methods such as the one presented here, that probe sample dynamics on the timescale of the driving pulse, are essential to understand the structural changes driven by X-ray heating.

This paper presents results from graphite samples irradiated by a high intensity ($\sim 10^{19}$ W/cm$^2$), ultrashort ($\sim 7$ fs) pulse of 9.86 keV X-rays, probed at a delay of up to 300 fs by a second pulse at 9.66 keV, such that the pump and probe diffraction lines are separated on the area detector. The diffraction signal from the sample changes significantly up to the maximum delay, with a strong loss of signal from diffraction peaks that probe order between planes of graphite, but a rise in signal from in-plane correlations.

## Experiment

The experiment was performed at Experimental Hutch 5, on BeamLine 3 of SACLA in Hyōgo, Japan [27,28]. This facility offers a two colour mode, where undulators upstream and downstream of an electron chicane are tuned to generate pulses at slightly different X-ray energies (9.86 and 9.66 keV, $\lambda$=1.257 and 1.283 Å, respectively) [29]. The energies were chosen to maximise pulse fluence, as SACLA lases most efficiently close to 10 keV, while still being either side of a k-edge (in this case, zinc at 9.659 keV), to allow the use of filtering to observe a single energy. The chicane is then used to delay the electrons, giving a corresponding delay between the pulses in the target chamber of up to 300 fs; since this moves the electron beam, the spatial overlap of the pulses from the undulators is checked after each change in delay. The pulses are 7 fs in duration (full width half maximum) with an energy of $120 \pm 30$ µJ at 0 fs delay; loss of electron beam quality in the chicane means that the probe pulse energy decreases with delay, with only 50% fluence at 300 fs. Together with beam focusing using Kirkpatrick-Baez mirrors for a elliptical spot size of 200 × 160 nm, we have an incident pump beam intensity (fluence) of $6.8 \pm 2.2 \times 10^{19}$ W/cm$^2$ ($4.8 \pm 1.6 \times 10^5$ J/cm$^2$). Due to the use of reflective, rather than refractive, focusing optics, the spot sizes of the two beams are identical and overlapped as long as the pulses are collinear as they leave the undulators, and there is only minimal signal outside the focal spot [30].

The X-ray pulses were incident on 20 µm thick graphite samples (density $\rho = 2.265$ g/cc), which had an inhomogeneous structure with the crystalline planes primarily oriented parallel to the surface. $\sim 1.5\%$ of the X-ray pulse energy is deposited by exciting photoelectrons which further collisionally ionize the target in a significantly larger area than the original focal spot [25]. Due to the long attenuation length of the X-rays through the graphite sample, the energy deposition did not vary significantly through the depth of the target, and the remaining energy is not absorbed. Electron cascades driven by the incoming beam were modelled using the XCASCADE-3D Monte-Carlo code [31], with the results shown in Fig. 2. Within the cascading time of $\sim 40$ fs, electron transport has diluted the absorbed dose down to 3–5 eV/atom by spreading it across an electron range of 1 µm, compared to 160 eV/atom if all absorbed energy is assumed to remain in the initial heating spot. The probed region therefore contains on the order of 1–3% of the absorbed energy after accounting for the electron transport. The heating Gaussian
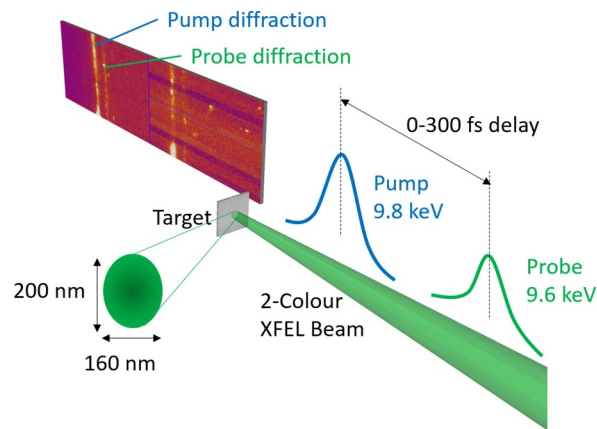


**Fig. 1.** Schematic of the setup in the experimental chamber, showing the two-colour focused beam entering from the XFEL, and the diffraction detection on the MPCCD. This view is rotated by 90°; in the experiment, the detector was located above the target, just outside the top of the chamber.
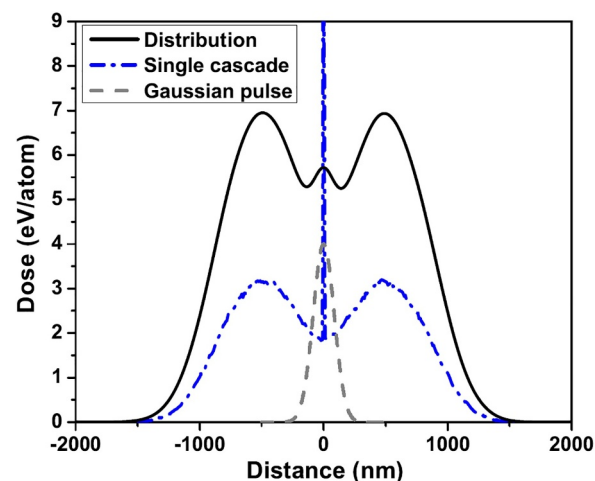


**Fig. 2.** Calculation of the heating range by the X-ray driven electron cascades. The dot-dashed line (blue) shows the range from a single cascade, while the solid line (black) shows the convolution of this with the focal spot size (dashed gray). The simulation assumes that all electrons are emitted parallel to the polarization; in reality they follow a cos$^2$ distribution, which might slightly reduce the calculated energy spread.

pulse, shown by the grey dashed line in Fig. 2, also indicates the region of the sample which is probed by the second pulse.

For each shot, the sample is irradiated by both the first (pump) pulse and the second (probe) pulse. The incoming XFEL spectrum is measured upstream of the experimental chamber, and the sum of the diffraction of both pulses is detected on a MultiPort Charged Couple Device (MPCCD) just outside the chamber [32], as shown schematically in Fig. 1. This measured signal allows the effect of changes in the ion structure to be observed in the diffraction pattern at a delay of up to 300 fs. The detector could be placed in different positions to cover different angular ranges, which were calibrated using copper samples.

## Results and discussion

The data from the MPCCD was integrated in the azimuthal direction and background subtracted; example lineouts, each averaged over > 300 shots, are shown in Fig. 3, with the diffraction orders highlighted and labeled with their respective Miller index (*hkl*). Due to the texture of the sample - which is analyzed in more detail in the Appendix - the (004) and (006) lines, found at 45° and 70°, are significantly weaker than would be expected from a powder sample. Our analysis focused on
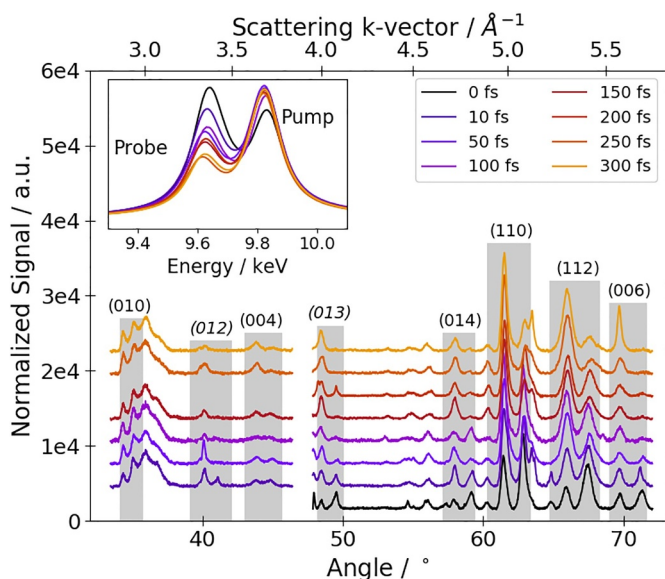
**Fig. 3.** Scattering lineout data from graphite, as a function of probing delay (earliest times at the bottom; colour online). The inset shows the corresponding incoming XFEL spectra, measured upstream of the experimental chamber. Signals were taken at two separate detector positions, with angular ranges 33˚-47˚ and 48˚-72˚. Each lineout is the average of around 300 shots. The scattering k-vectors are calculated for the probe pulse (9.66 keV, $\lambda$=1.283 Å). For each highlighted diffraction order, there is signal from both the pump and probe pulse. The diffraction lines (012) and (013) are not analysed in the subsequent figure, but show comparable behaviour.

pairs of specific peaks from the pump and probe pulses. The change in diffraction intensity was calculated from the signal by fitting Gaussian peaks to the two energies in the incoming XFEL beam spectrum (shown in the inset of Fig. 3) and the two peaks in the diffraction lineout corresponding to the pump and probe diffraction from the same order. The signal ratio, *k*, was then calculated from the ratio of the normalized intensities, as in the work of Inoue et al. [33]:

$$k = \frac{probe_{out}}{probe_{in}} \bigg/ \frac{pump_{out}}{pump_{in}}. \tag{1}$$

This calculates the drop in signal from the probing beam normalized to the diffraction efficiency of the pump beam. It assumes that there is no change in lattice structure on the timescale of the pump pulse, and that, since the pump and probe diffract from the same point on the sample, the texture for a given shot is effectively identical for both pulses.

Fig. 4 shows the changes in the signal ratios as a function of delay. Since data was not taken at the lower angle MPCCD position for delays of 0 fs and 200 fs, there are no points at this delay for the (010) and (004) lines. The most striking difference is between the in-plane – (010) at 34.5˚ and (110) at 62.0˚ – and out-of-plane lines. The latter, with non-zero components between graphite planes (Miller index $l \neq 0$) show a very strong drop in the first 10 fs, and continue with a slower decline over the rest of the delays. On the other hand, the in-plane diffraction orders show a rise in signal across the measured delays, albeit with significant uncertainties at late times. Such differences in the signal changes between different diffraction peaks are expected for non-thermal melting [34], although recent research has also predicted such results for thermal melting in silicon [35]. In all cases, there is significant variation between measurements, primarily due to the texture of the samples varying strongly between points, and the very small spot size making the diffraction sensitive to the effect of crystallites.

The effect of direct ionization reducing the diffraction signal is estimated to be minimal. Less than 1% of the atoms in the focal spot are
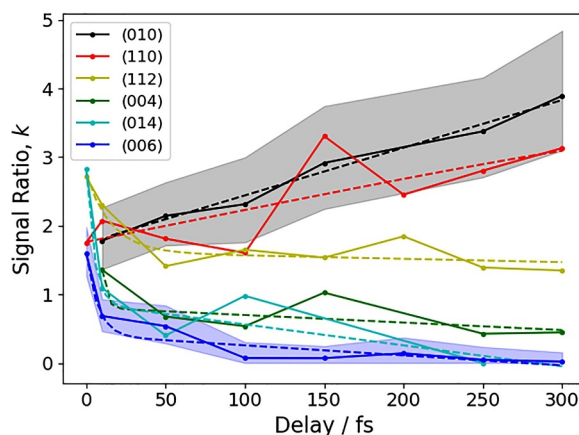


**Fig. 4.** Changes in the value of the scattering ratio with time for different graphite diffraction peaks; the ratios are calculated from the averaged lineouts shown in Fig. 3. As examples, the shaded regions around the (010) and (006) lines indicate the level of uncertainty at each time delay, estimated from the range of the fitting parameters; as a proportion of the signal, these generally increase with delay. The diffraction lines with no out-of-plane correlations show distinctly different behaviour to the other peaks.

ionized by the initial pump pulse, and although the cascading photo-electron can subsequently ionize many more, this will mostly occur over a much wider area, due to the long range of the photoelectrons. Such a small ionization fraction will make a negligible difference to the diffraction signal [36], and therefore the observed drops in signal must be explained by changes in the ionic structure due to the absorbed energy.

A precise characterization of the structural changes induced by the X-ray heating in this experiment is challenging, due to the small range of *k*-vectors that are probed by the detector (covering around 9˚ of the Debye-Scherrer ring), and the highly textured initial sample (with mosaicity between crystallites on the order of 18˚; the method of characterizing this is found in the Appendix). Although the drop in signal from the interplanar lines implies a disordering, the continuing presence of signal from the in-plane lines requires that the graphite sheets remain intact. We therefore propose that the disordering proceeds by increasing the mosaicity, both between and within crystallites, as the bonds between the planes are broken by the heating. A sketch of this proposed interpretation is illustrated in Fig. 5a).

In the case of a perfect crystal – green in Fig. 5 – one can only get a Bragg peak, rather than a Debye-Scherrer ring.The blue case illustrates the initial mosaicity of our sample, with a FWHM in the distribution of plane angles $\beta$ equal to 18˚. With X-ray heating, the mosaicity increases, either by a loss of coherence between the planes, or the planes themselves buckling, illustrated in the red cases. For both, the atoms within the planes become more weakly correlated with those in neighboring planes, causing lines with $l \neq 0$ to weaken, with a greater effect for higher *l*. However, the average separation between the planes is initially unchanged, as this would cause a shift of the interplanar peak positions along the *k* direction, equivalent to a change in diffraction angle, which is not observed on these timescales. The effect on the in-plane peaks is more complex: since only planes with angles on the wings of the distribution give signal, due to the scattering geometry, the increase in mosaicity means that a larger number of crystallite planes are found at this angle, causing an increase in signal from all diffraction lines. Since the increase is only observed for the (hk0) diffraction lines, the effect must be smaller than the signal loss associated with disordering between the planes; in the case of the (112) line, the two effects appear to almost cancel out. From the (010) and (110) lines, we estimate that the observed signal increases would require the mosaicity to rise from 18˚ to ~ 23˚, but we emphasise that this explanation is still only speculative, and would require a larger detector, and a
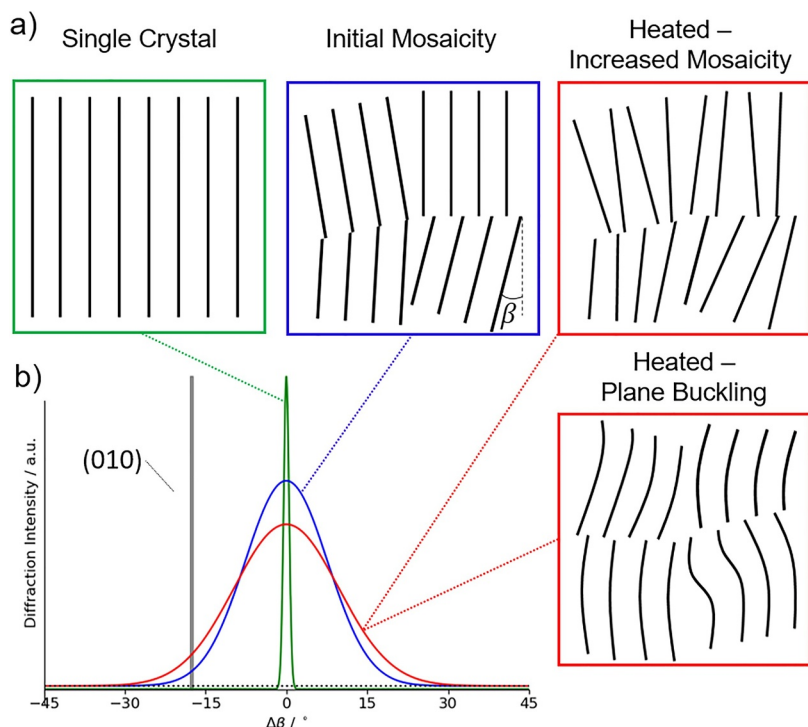
Fig. 5. The effect of changing planar distributions on the diffraction intensity for mosaic crystals. a) Cartoons of the planar distributions, with the two heated examples giving possible explanations for the proposed increase in mosaicity. In both examples, the change in mosaicity is exaggerated for clarity. b) Distribution of the plane angles $\beta$, relative to the single crystal orientation, for each of the mosaicity cases. For example, planes at an angle of -17.6° from the vertical have (010) diffraction vectors that overlap with the scattering vector in the experimental geometry. As the mosaicity increases, more of the planes are at this angle, giving an increase in signal.

different experimental geometry, to be confirmed in a future experiment.

After the experiment, we used optical and scanning electron microscopy to examine the holes generated by the XFEL beams. Unlike the diffraction measurements, these are due to the heating effect of both the pump and probe beams. Examples of holes in graphite measured by scanning electron microscope (SEM), taken from the front (incident) and rear (detector) sides, are shown in Fig. 6. The hole sizes vary significantly between shots, and are only weakly correlated to the variation in total X-ray fluence. On average, the hole size at the surface appears to be slightly larger than the range of the generated photoelectrons in the sample, with the calculation shown in Fig. 2 giving a heated region of diameter 3 μm compared to an average surface hole size of 5.3 μm. Both of these values are much larger than the focal spot size, which was measured with a wire scan as having a 200 nm diameter. The holes appear to narrow with depth which may imply the presence of surface effects, and that the hole size deeper in the sample better reflects the lateral electron energy deposition. This would also suggest that, even over the timescales of bulk damage, the region of the target which is heated above the damage threshold is not significantly larger than the initial range of the excited photoelectrons, although much larger than the incident spot size.

Comparing the results to previous experimental work, the most obvious parallel is the work of Hau-Riege et al. [20], which used a single X-ray pulse to both melt and probe a graphite sample. By observing the diffraction intensity from the (002) diffraction line, they inferred both a rapid increase in ion temperature, and significant ionization ($Z_f > 0.8$) from the decreasing signal with longer pulses. Since they observed an interplanar line, the drop in signal appears to be in agreement with our results, however it was achieved with much higher absorbed energy fluences; their pulse energies were as high as 2 mJ, and the X-ray energy was 2 keV, for higher absorption. Their much larger spot sizes (a few μm in diameter) also mean that the heating from the subsequent Auger cascades affect the signal within the spot, in contrast to this work, where a majority of the energy leaves the probed region. Taking these effects into account, we estimate energy densities at the front surface of their probed spot to be on the order of 50 eV/atom after the Auger cascades, so at least 10x higher than in our

experiment. This means that their use of the plasma-based Debye-Hückel model to calculate an ion temperature may be appropriate. In our experiment, with lower energy density and the continuing presence
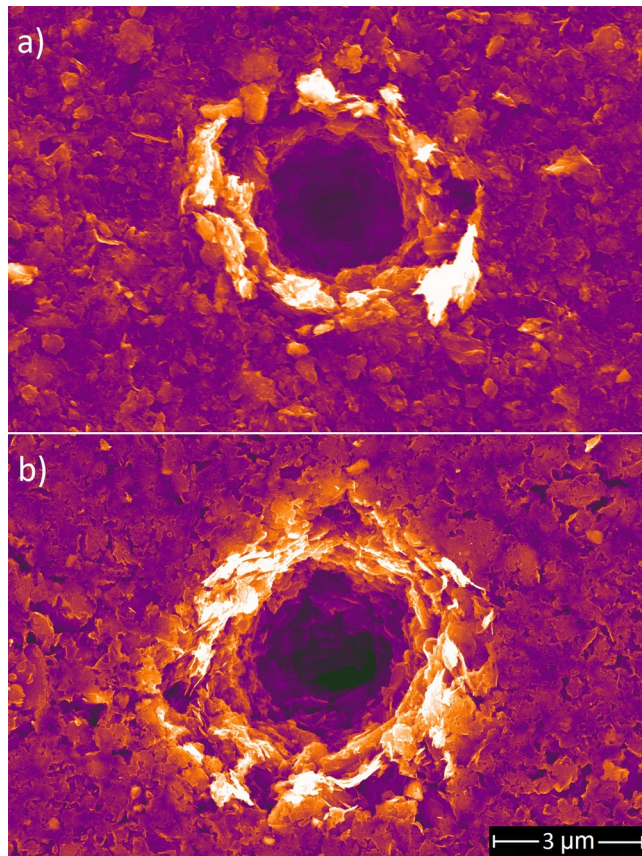


Fig. 6. Images of holes in the graphite sample on the (a) incident and (b) exit side, taken with a Scanning Electron Microscope (SEM).

of covalent bonding, it clearly would not.

Turning to theoretical work, there exist various approaches to simulating the behaviour of X-ray heated matter. The tight binding molecular dynamics (MD) work of Jeschke at al. [37] predicts that damage in graphite can proceed by the removal of intact graphite sheets, as seems to be observed here, although their simulations were performed with a slightly lower absorbed energy (2–3 eV/atom). Only at higher absorbed energies, the theory predicts that the planes themselves would break apart, such that signal from both in- and out-of- plane diffraction peaks would be lost on ultrafast timescales. The same tight binding approach has been used in the hybrid XTANT (X-ray-induced Thermal And Nonthermal Transitions) model of Medvedev et al. [38], in combination with Monte Carlo photon absorption and Boltzmann collisions for the electron-ion energy exchange. This has been used to describe thermal and nonthermal melting in silicon [39], graphitization [40] and anisotropic disordering [41] in diamond, and may be similarly able to reproduce the phenomena observed here.

Other approaches include Molecular Dynamics in combination with Density Functional Theory, which has previously been used to simulate the behaviour of samples with high electron temperatures and low ion temperatures (see e.g. [42,43]). Although time-dependent approaches can model non-thermal electron energy distributions [44], such as what we expect from the X-ray heating, they are very computationally expensive [45]. At the other extreme, Particle in Cell (PIC) codes can directly simulate the photoionization and electron cascade behaviour driven by hard X-rays [46,47], and are showing progress towards the inclusion of ionization dynamics [48]. However, they cannot account for the ion structure, which our results suggest to be a hugely important effect.

## Conclusion

Under high intensity X-ray irradiation, sample heating proceeds by excitation of photoelectrons, which deposit their energy across a wide area by driving Auger cascades; this is confirmed by examination of the sample after the experiment, which shows damage within the photo-electron range. After heating, graphite rapidly loses interplanar order, while the planes remain intact up to 300 fs – longer than the timescale of previously observed nonthermal melting processes. The apparent increase in diffraction signal from in-plane orders may be due to the induced interplanar disordering causing an increase in the sample mosaicity, and therefore a larger number of scattering planes, but further experiments are needed to confirm this. Previously published simulations agree with our results, suggesting that, at similar levels of heating to those reached here, damage may proceed by the removal of intact planes due to breaking of interplanar bonds, while the bonds within the planes are not broken [37]. Our results demonstrate the significance of the lattice structure in predicting the evolution of rapidly heated samples, and the complexity of X-ray heating as a method for generating high energy density states. Future pump-probe experiments with significantly longer delays, enabled by the X-ray split and delay line [49], may be able to bridge the gap between the initial disordering observed here and the long term evolution and bulk damage.

## Appendix A. Sample Texture

To investigate the initial microscale structure of the graphite sample, x-ray diffraction (laboratory) measurements were carried out using an Empyrean / Panalytical diffractometer with a Cu-target source ($\lambda$ = 1.54055Å). On the source side the setup was equipped with a Göbel mirror to enhance the brilliance. An area-Pixel-Detector (516 x 516 pixels with 55 μm pixel size) that is able to cover more than 6° in two directions was used to record two dimensional diffraction images in transmission and reflection mode as well as several pole figures at two selected reflections (002, 112). Diffraction data was taken in transmission and reflection geometry, shown schematically in Fig. A1, with the resulting line scans shown in Fig. A2. There is a clear difference between the $\theta - 2\theta$ measurement in reflection and and the $2\theta$ measurement in transmission mode. Most of the peaks can be attributed to graphite (PDF: 00-56-159). The reflection measurement shows strong (00$l$) peaks indicating a strong (001) texture i.e. the planes are parallel to the surface. However, a comparison of the diffraction and transmission measurements reveals the existence of additional carbon phases within the volume of the sample. By comparing the intensities of the (002) peak, we estimate that around 1% of the signal comes from a powder-like phase. Ignoring the texture, an average crystallite size of around 10 nm was derived from a simple line analysis of both measurements.

Fig. A3 shows the two pole figures and the corresponding line profiles, integrated along $\phi$. The preferential (001) orientation is confirmed, although with a very broad distribution of plane angles, corresponding to a mosaicity of 18°.
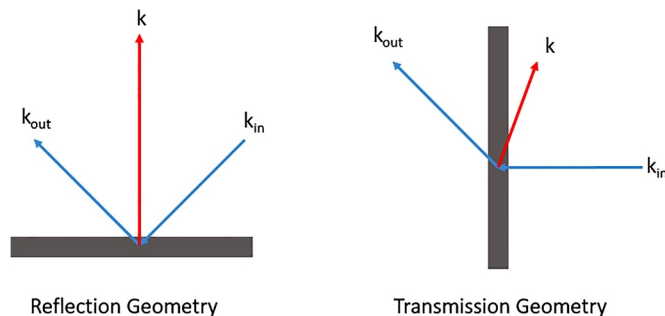


**Fig. A1.** Diffraction geometries for the sample analysis setup, with the scattering vector $k = k_{out} - k_{in}$ marked.
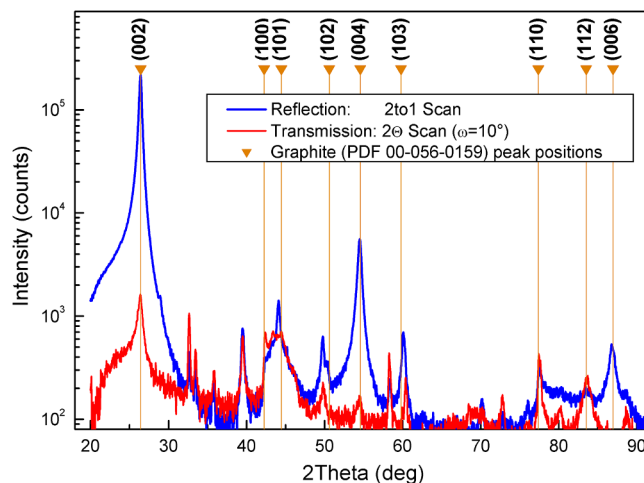
**Fig. A2.** Line profiles of the diffraction measurements in transmission (red) and reflection (blue) geometry. The graphite Bragg reflection peaks are marked by arrows and labelled. The large increase in signal from the (00*l*) diffraction orders in reflection geometry is indicative of the sample texture.
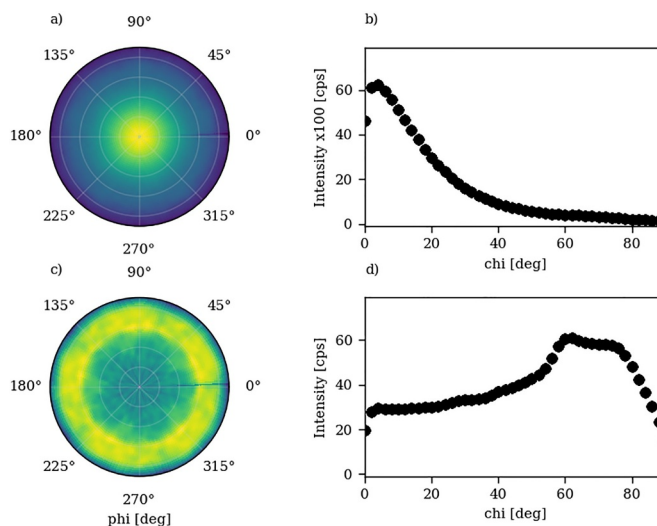


**Fig. A3.** Pole figures (a,c) and line profiles integrated along phi (b,d) of the (002) reflection (a,b) and of the (112) reflection (c,d). Both measurement show a broad intensity distribution and a non zero background that can be attributed to the low amount of powder like material.

## References

[1] C.W. Siders, et al., Detection of nonthermal melting by ultrafast X-ray diffraction, Science 286 (1999) 1340–1342.

[2] K. Sokolowski-Tinten, et al., Femtosecond X-ray measurement of ultrafast melting and large acoustic transients, Phys. Rev. Lett. 87 (2001) 225701.

[3] A. Rousse, et al., Non-thermal melting in semiconductors measured at femtosecond resolution, Nature 410 (2001) 65–68.

[4] T. Choi, C. Grigoropoulos, Observation of femtosecond laser-induced ablation in crystalline silicon, J. Heat Transf. 126 (2004) 723–726.

[5] B. Rethfeld, Modelling ultrafast laser ablation, J. Phys. D 50 (2017) 193001.

[6] E.G. Gamaly, The physics of ultra-short laser interaction with solids at non-relativistic intensities, Phys. Rep. 508 (2011) 91–243.

[7] D. von der Linde, K. Sokolowski-Tinten, J. Bialkowski, Laser–solid interaction in the femtosecond time regime, Appl. Surf. Sci. 109–110 (1997) 1–10.

[8] B. Rethfeld, A. Kaiser, M. Vicanek, G. Simon, Ultrafast dynamics of nonequilibrium electrons in metals under femtosecond laser irradiation, Phys. Rev. B 65 (2002) 214303.

[9] J.K. Chen, W.P. Latham, J.E. Beraun, The role of electron–phonon coupling in ultrafast laser heating, J. Laser Appl. 17 (2005) 63.

[10] B. Monserrat, R.J. Needs, Comparing electron-phonon coupling strength in diamond, silicon, and silicon carbide: First-principles study, Phys. Rev. B 89 (2014) 1–8.

[11] K. Sokolowski-Tinten, et al., Transient states of matter during short pulse laser ablation, Phys. Rev. Lett. 81 (1998) 224–227.

[12] A. Vailionis, E.G. Gamaly, V. Mizeikis, W. Yang, A.V. Rode, S. Juodkazis, Evidence of superdense aluminium synthesized by ultrafast microexplosion, Nat. Commun. 2 (2011) 445–446.

[13] T. Kluge, et al., Using X-ray free-electron lasers for probing of complex interaction dynamics of ultra-intense lasers with solid matter, Phys. Plasmas 21 (2014) 033110.

[14] D. Kraus, et al., Characterizing the ionization potential depression in dense carbon plasmas with high-precision spectrally resolved X-ray scattering, Plasma Phys. Controll. Fusion 61 (2018) 014015.

[15] H. Yumoto, et al., Focusing of X-ray free-electron laser pulses with reflective optics, Nat. Photonics 7 (2013) 43–47.

[16] H. Mimura, et al., Generation of 1020 W cm-2 hard X-ray laser pulses with two-stage reflective focusing system, Nat. Commun. 5 (2014) 3539.

[17] S.M. Vinko, et al., Creation and diagnosis of a solid-density plasma with an X-ray free-electron laser, Nature 482 (2012) 59–62.

[18] K.R. Beyerlein, et al., Ultrafast nonthermal heating of water initiated by an X-ray Free-Electron Laser, Proc. Natl. Acad. Sci. 6 (2018) 201711220.

[19] C.A. Stan, et al., Liquid explosions induced by X-ray laser pulses, Nat. Phys. 12 (2016) 966–971.

[20] S. Hau-Riege, et al., Ultrafast transitions from solid to liquid and plasma states of graphite induced by X-Ray free-electron laser pulses, Phys. Rev. Lett. 108 (2012) 217402.

[21] F. Tavella, et al., Soft x-ray induced femtosecond solid-to-solid phase transition, High Energy Density Phys. 24 (2017) 22–27.

[22] M. Makita, et al., Femtosecond phase-transition in hard x-ray excited bismuth, Sci. Rep. 9 (2019) 602.

[23] S.K. Sundaram, E. Mazur, Inducing and probing non-thermal transitions in semiconductors using femtosecond laser pulses, Nat. Mater. 1 (2002) 217–224.

[24] B. Ziaja, R.A. London, J. Hajdu, Unified model of secondary electron cascades in diamond, J. Appl. Phys. 97 (2005) 064905.

[25] A.N. Grum-Grzhimailo, et al., On the size of the secondary electron cloud in crystals

irradiated by hard X-ray photons, Eur. Phys. J. D 71 (2017) 69.

[26] M. Lyon, S.D. Bergeson, G. Hart, M.S. Murillo, Strongly-coupled plasmas formed from laser-heated solids, Sci. Rep. 5 (2015) 15693.

[27] M. Yabashi, H. Tanaka, T. Ishikawa, Overview of the SACLA facility, J. Synchrotron Radiat. 22 (2015) 477–484.

[28] K. Tono, et al., Beamline, experimental stations and photon beam diagnostics for the hard x-ray free electron laser of SACLA, New J. Phys. 15 (2013) 083035.

[29] T. Hara, et al., Two-colour hard X-ray free-electron laser with wide tunability, Nat. Commun. 4 (2013) 2919.

[30] T. Pikuz, et al., 3D visualization of XFEL beam focusing properties using LiF crystal X-ray detector, Sci. Rep. 5 (2015) 17713.

[31] V. Lipp, N. Medvedev, B. Ziaja, Classical Monte-Carlo simulations of x-ray induced electron cascades in various materials, in Damage to VUV, EUV, and X-ray Optics VI 10236 International Society for Optics and Photonics, 2017, p. 102360H.

[32] T. Kameshima, X-ray two-dimensional detector with a multi-port charge-coupled device for X-ray free electron laser experiments, (2014).

[33] I. Inoue, et al., Observation of femtosecond X-ray interactions with matter using an X-ray-X-ray pump-probe scheme, Proc. Natl. Acad. Sci. 113 (2016) 1492–1497.

[34] T. Zier, Signatures of nonthermal melting, Struct. Dyn. 2 (2015) 054101.

[35] N. Medvedev, Femtosecond x-ray diffraction can discern nonthermal from thermal melting, Phys. Rev. B 99 (2019) 100303.

[36] S.P. Hau-Riege, X-ray atomic scattering factors of low- Z ions with a core hole, Phys. Rev. A 76 (2007) 1–5.

[37] H.O. Jeschke, M.E. Garcia, K.H. Bennemann, Theory for the ultrafast ablation of graphite films, Phys. Rev. Lett. 87 (2001) 015003.

[38] N. Medvedev, V. Tkachenko, V. Lipp, Z. Li, B. Ziaja, Various damage mechanisms in carbon and silicon materials under femtosecond x-ray irradiation, 4open 1 (2018)

1–23.

[39] N. Medvedev, Z. Li, B. Ziaja, Thermal and nonthermal melting of silicon under femtosecond x-ray irradiation, Phys. Rev. B 91 (2015) 054113.

[40] N. Medvedev, H.O. Jeschke, B. Ziaja, Nonthermal phase transitions in semiconductors induced by a femtosecond extreme ultraviolet laser pulse, New J. Phys. 15 (2013) 015016.

[41] N. Medvedev, B. Ziaja, Multistep transition of diamond to warm dense matter state revealed by femtosecond X-ray diffraction, Sci. Rep. 8 (2018) 5284.

[42] J. Vorberger, D.O. Gericke, Coupled mode effects on energy transfer in weakly coupled, two-temperature plasmas, Phys. Plasmas 16 (2009) 082702.

[43] J. Vorberger, D.O. Gericke, Comparison of electron-ion energy transfer in dense plasmas obtained from numerical simulations and quantum kinetic theory, High Energy Density Phys. 10 (2014) 1–8.

[44] D.A. Chapman, D.O. Gericke, Analysis of Thomson scattering from nonequilibrium plasmas, Phys. Rev. Lett. 107 (2011) 165004.

[45] A.D. Baczewski, X-ray Thomson Scattering in Warm Dense Matter without the Chihara Decomposition, Phys. Rev. Lett. 116 (2016) 1–6.

[46] Y. Sentoku, Kinetic effects and nonlinear heating in intense x-ray-laser-produced carbon plasmas, Phys. Rev. E 90 (2014) 051102.

[47] R. Royle, Kinetic modeling of X-ray laser-driven solid Al plasmas via particle-in-cell simulation, Phys. Rev. E 95 (2017) 063203.

[48] L.G. Huang, T. Kluge, T.E. Cowan, Dynamics of bulk electron heating and ionization in solid density plasmas driven by ultra-short relativistic laser pulses, Phys. Plasmas 23 (2016) 063112.

[49] W. Lu, et al., Development of a hard X-ray split-and-delay line and performance simulations for two-color pump-probe experiments at the European XFEL, Rev. Sci. Instrum. 89 (2018) 063121.